

Computational Materials Science

Generalized stacking fault energies and Peierls stresses in refractory body-centered cubic metals from machine learning-based interatomic potentials

--Manuscript Draft--

Manuscript Number:	
Article Type:	Full Length Article
Section/Category:	Atomic Description
Keywords:	Spectral neighbor analysis potential; generalized stacking fault energy; Peierls stress; refractory body-centered cubic metals
Corresponding Author:	Xiaowang Wang Santa Barbara, California UNITED STATES
First Author:	Xiaowang Wang
Order of Authors:	Xiaowang Wang Shuozhi Xu Wu-Rong Jian Xiang-Guo Li Irene Beyerlein
Abstract:	The generalized stacking fault energies (GSFE) and Peierls stresses are strongly related to the mechanical properties of refractory metals. In this work, the GSFE curves and Peierls stresses of screw and edge dislocations in four body-centered cubic refractory metals (Mo, Nb, Ta, and W) on the {110}, {112}, and {123} slip planes are calculated using molecular statics simulations. A recently developed machine learning (ML)-based interatomic potential, called the spectral neighbor analysis potential (SNAP), is employed in all simulations. The computed GSFE curves achieve reasonable agreement with those from ab initio calculations and predict the asymmetry with respect to sense of glide direction on the {112} and {123} planes better than non-ML interatomic potentials. In general, SNAP provides screw dislocation Peierls stresses close to those of density functional theory, closer than those achieved by non-ML potentials. The screw dislocation Peierls stress values confirm slip symmetry on the {110} plane and exhibit pronounced slip asymmetry on the {112} and {123} planes. For all metals, the edge dislocation Peierls stress are the lowest on the {110} plane and the highest on the {112} plane. For screw dislocations, glide on either the {110} or the {123} plane is the easiest.
Suggested Reviewers:	Liming Xiong Iowa State University lmxiong@iastate.edu Prof. Xiong is an expert who focuses on the deformation mechanisms of metallic materials and computational materials science. Caizhi Zhou University of South Carolina caizhi@mailbox.sc.edu Prof. Zhou is an expert who focuses on the deformation mechanisms of metallic materials and computational materials science. Garrett Tucker Colorado school of mines tucker@mines.edu Prof. Tucker is an expert who focuses on the deformation mechanisms of metallic materials and computational materials science.



University of California, Santa Barbara

Santa Barbara, California 93106, USA

www.ucsb.edu

November 30, 2020

Dear Editor of *Computational Materials Science*,

On behalf of my co-authors, Shuzhi Xu, Wu-Rong Jian, Xiang-Guo Li, and Irene J. Beylerlein, I am submitting the following manuscript entitled “Generalized stacking fault energies and Peierls stresses in refractory body-centered cubic metals from machine learning-based interatomic potentials” to be considered for publication into *Computational Materials Science*. We confirm that this work is original and has neither been published elsewhere nor is currently under consideration for publication elsewhere. We declare no conflict of interest.

In this work, we study the generalized stacking fault energies (GSFE) and Peierls stresses in Mo, Nb, Ta, and W via atomic scale calculations using machine learning (ML)-based spectral neighbor analysis potentials. The GSFE are surplus energies that arise from the shift of one half of the crystal with respect to the other half. The Peierls stress is the minimum resolved shear stress required to translate a dislocation in a crystal. Both quantities are considered among the most important factors controlling plastic deformation of metals. Numerous studies have been dedicated to obtaining accurate, reliable values for the GSFE and Peierls stress in a wide variety of materials. However, most prior atomistic simulations used non-ML based, classical interatomic potentials, and the accuracy in those results is not satisfactory compared with more accurate, but also more costly, *ab initio* calculations. Since the ML-based interatomic potentials are more accurate than the classical ones, it is important to use them to calculate the two important quantities in a series of refractory metals that can sustain high temperatures. As a result, we believe this manuscript lies within the scope of *Computational Materials Science*.

On behalf of my co-authors, I thank you for considering our work for potential publication in *Computational Materials Science*. Please do not hesitate to contact me should you have any questions or need more information.

Sincerely yours,
 Wangxiao Wang,
 Department of Physics
 University of California, Santa Barbara
 E-mail: xiaowangwang@ucsb.edu

1
2
3
4
5
6
7
8
9

Generalized stacking fault energies and Peierls stresses in refractory body-centered cubic metals from machine learning-based interatomic potentials

Xiaowang Wang^{a,*}, Shuzhi Xu^b, Wu-Rong Jian^b, Xiang-Guo Li^c, Irene J. Beyerlein^{b,d}

^a*Department of Physics, University of California, Santa Barbara, CA 93106-9530, USA*

^b*Department of Mechanical Engineering, University of California, Santa Barbara, California 93106-5070,
USA*

^c*Department of Materials Science and Engineering, University of Wisconsin, Madison, WI 53706, USA*

^d*Materials Department, University of California, Santa Barbara, California 93106-5050, USA*

Abstract

The generalized stacking fault energies (GSFE) and Peierls stresses are strongly related to the mechanical properties of refractory metals. In this work, the GSFE curves and Peierls stresses of screw and edge dislocations in four body-centered cubic refractory metals (Mo, Nb, Ta, and W) on the {110}, {112}, and {123} slip planes are calculated using molecular statics simulations. A recently developed machine learning (ML)-based interatomic potential, called the spectral neighbor analysis potential (SNAP), is employed in all simulations. The computed GSFE curves achieve reasonable agreement with those from *ab initio* calculations and predict the asymmetry with respect to sense of glide direction on the {112} and {123} planes better than non-ML interatomic potentials. In general, SNAP provides screw dislocation Peierls stresses close to those of density functional theory, closer than those achieved by non-ML potentials. The screw dislocation Peierls stress values confirm slip symmetry on the {110} plane and exhibit pronounced slip asymmetry on the {112} and {123} planes. For all metals, the edge dislocation Peierls stress are the lowest on the {110}

*Corresponding author

Email address: xiaowangwang@ucsb.edu (Xiaowang Wang)

1
2
3
4
5
6 plane and the highest on the {112} plane. For screw dislocations, glide on either the {110}
7 or the {123} plane is the easiest.
8
9

10 *Keywords:* Spectral neighbor analysis potential; generalized stacking fault energy;
11 Peierls stress; refractory body-centered cubic metals

12
13
14
15 **1. Introduction**
16
17

18 Refractory metals are metals with high melting points (above 2200 °C) [1] and the
19 ability to retain ultra-high strengths under elevated temperatures [2]. This combination of
20 properties makes them desirable materials for a wide range of industrial applications. One
21 of the earliest and most well-known of these applications is the use of W in incandescent
22 lighting [3]. Today, refractory metals are present in many cutting-edge technologies as
23 components exposed to extreme environments [4]. Refractory metals, for example, can
24 serve as control rods in nuclear energy reactors [5]. They also find application in rocket
25 engines, which must sustain the high temperatures from burning rocket fuels. The main
26 engine of Apollo Lunar Modules, for instance, consists of 89% Nb [6].
27
28

29 While the high temperature strength of refractory metals makes them attractive struc-
30 tural materials, it also renders them difficult to shape into useful industrial components
31 [7]. Plastic behavior in metals is realized by the glide of dislocations on specific crys-
32 tallographic slip systems or slip modes, and for refractory metals, the stresses required
33 to activate dislocation glide are relatively high compared to traditional metals like steel or
34 aluminum [8]. Dislocation motion involves the breaking and forming of bonds across their
35 crystalline glide planes, roughly similar to shearing the two halves of the crystal across the
36 plane [9]. The potential energy associated with shearing is the generalized stacking fault
37 energy (GSFE) [10], and from GSFE calculations, a measure of the ideal shear strength
38 can be obtained for the plane [11]. Another basic measure of dislocation glide resistance
39 is the Peierls stress, the minimum resolved shear stress required for an isolated, stationary
40
41

dislocation to first move [12]. In some cases, the GSFE and Peierls stress can be related [13]. A study on body-centered cubic (BCC) Fe demonstrated how variations in the GSFE affected the core structure of the edge character dislocations [14].

Plastic deformation in refractory metals may possibly occur by multiple distinct slip planes, commonly the {110}, {112}, and {123} planes [15]. To date, studies on Peierls stresses of refractory metals often focused on the {110} plane and less so on the {112} plane. No studies have computed the Peierls stress for the {123} plane. Obtaining key insights into the deformation behavior refractory metal components would benefit from a comprehensive understanding of how these critical energies and stresses vary with crystallographic glide plane and dislocation character.

Common methods for characterizing dislocation structures and their behavior are atomic-scale simulation methods, such as density functional theory (DFT) and molecular statics (MS) and dynamics (MD) calculations. DFT is the most accurate of the three methods and has been used in a few studies to calculate GSFE curves in the ⟨111⟩ direction on the {110} plane and, in few cases, the {112} plane, for six refractory BCC metals: Cr [16], Mo [16, 17], Nb [16, 18, 19], Ta [16, 20], V [16, 21], and W [16, 22–26]. Peierls stress calculations via DFT for the {110} and {112} planes have also been carried out for all these metals: Cr [27], Mo [28–32], Nb [31, 33], Ta [29, 31, 33, 34], V [31, 33], and W [22, 31–33]. DFT calculations are usually limited to a relatively small number of atoms, in the range of 10–200 atoms. MS or MD simulations, on the other hand, can be used to study dislocation behavior in model crystals of much larger size scales [35], although with less accuracy due to the reliance on interatomic potentials [34, 36]. In this regard, many of the commonly used interatomic potentials, such as the embedded-atom method (EAM) and the Finnis-Sinclair (F-S) potentials, have been found to have a few issues [37, 38]. Classical interatomic potentials have been shown to perform poorly in calculating Peierls stress in BCC metals, producing values more than 100% greater than DFT calculations

1
2
3
4
5
6 due to omission of quantum effects [39]. For BCC Fe, properties, such as energies of
7 defective configurations, Peierls potentials associated with screw dislocations, and other
8 fundamental bulk properties are not satisfactorily reproduced by EAM and F-S potentials
9 [40].
10
11

12 Recently, machine learning (ML)-based interatomic potentials have emerged as a new
13 class of potentials and are rapidly gaining popularity [41]. Similar to classical interatomic
14 potentials, ML potentials incorporate quantum effects only in the construction of the po-
15 tential. However, ML potentials attempt to remedy the loss of accuracy through opti-
16 mization of potential function parameters through an ML algorithm [42]. Unlike classical
17 interatomic potentials, physical approximations are not used other than in the reference
18 electronic structure during its construction stage. ML potentials have achieved near DFT
19 accuracy in calculating material properties with computational cost more than one order
20 of magnitude lower [43].
21
22

23 Several kinds of ML potentials have been used for atomistic simulations [44], including
24 the high-dimensional neural network potential (NNP), spectral neighbor analysis potential
25 (SNAP), Gaussian approximation potential (GAP), and moment tensor potential (MTP).
26 They differ in accuracy, computational cost, and training difficulty. In developing an ML
27 potential for a new material, training sets that span a wide variety of conditions are used to
28 allow the potential to learn and improve through ML algorithm. An effective ML algorithm
29 means less training difficulty in that less training simulations need to be performed for
30 the potential to achieve a certain accuracy. Under these criteria, the most accurate ML
31 potentials are the GAP and MTP potentials. However, SNAP exceeds GAP in having lower
32 computational cost and exceeds MTP in having higher extrapolability [45]. In addition,
33 SNAP has been shown to reach reasonable accuracy, while requiring less training data
34 when fitting a new material [46].
35
36

37 In this paper, we use atomistic simulations employing the SNAP ML potential [47] to
38
39

calculate the GSFE curves and Peierls stresses for edge and screw dislocations on three
{110}, {112}, and {123} planes in Mo, Nb, Ta, and W. We demonstrate that on all three
planes, the GSFE curves from SNAP agree well with those from DFT. We show that the
group VI Mo and W metals achieve higher peak energies in the GSFE curves compared to
the group V Nb and Ta metals. In addition, we show that for edge dislocations, the Peierls
stress are the lowest on the {110} plane and the highest on the {112} plane. For screw
dislocations, however, glide on either the {110} or {123} plane is the easiest. Our results
confirm the twinning/anti-twinning slip asymmetry in screw dislocation Peierls stress in
the {112} plane. We reveal that like the {112} plane, the highest order {123} plane also
exhibits glide asymmetry. The differences in screw-to-edge Peierls stress ratio and slip-
plane anisotropy among these four metals are also discussed.

2. Basic structural parameters

We first validate SNAP against DFT by calculating the lattice parameter a_0 and three elastic constants (C_{11} , C_{12} , C_{44}) associated with each BCC metal. To calculate a_0 , a series of periodic simulation cells of different sizes is constructed. The bulk energy of each cell is computed and a_0 is obtained for the cell with the lowest energy [48]. The C_{11} , C_{12} , C_{44} are obtained using the stress-strain method [49]. The list of results in Table 1 demonstrates that the SNAP a_0 agrees well with that from DFT. Similarly, the SNAP elastic constants achieve good agreement with the DFT constants, differing by less than 10%. Based on these results, we proceed with confidence to use SNAP to calculate the GSFE and Peierls stresses for these four refractory metals. LAMMPS [50] is used for all MS simulations that follow.

Table 1: Lattice parameters a_0 (in Å) and elastic constants C_{11} , C_{12} , and C_{44} (in GPa). The isotropic shear modulus in Hill form, μ , is calculated based on C_{11} , C_{12} , and C_{44} . DFT results are from Ref. [16].

	Method	Mo	Nb	Ta	W
a_0	SNAP	3.167	3.326	3.317	3.181
	DFT	3.16	3.324	3.32	3.184
C_{11}	SNAP	434.85	266.09	256.79	560.28
	DFT	467.85	249.01	268.13	520.35
C_{12}	SNAP	169.16	142.57	160.86	217.81
	DFT	158.75	135.43	160.35	199.88
C_{44}	SNAP	95.87	20.3	66.21	154.64
	DFT	100.22	18.1	77.38	142.42
μ	SNAP	109.27	32.32	58.19	161.08
	DFT	119.29	29.23	66.94	149.3

1
2
3
4
5
6 **3. Generalized stacking fault energy**
7
8
9
10

11 *3.1. Methodology*
12
13
14
15
16
17
18
19
20
21
22
23
24
25
26
27
28
29

With SNAP, we calculate GSFE curves using a method similar to that used in Ref. [49]. Simulation cells are first constructed with a 12 Å vacuum on one end in the y direction to prevent periodic images from interacting with each other. BCC crystal lattice structures are then created inside the simulation cells (except the vacuum region). For each metal, three different lattice orientations are adopted by making the x - z plane correspond to the glide plane of interest. For the {110} plane calculation, the orientation of the crystal is set to be $x\langle 112 \rangle$, $y\langle 110 \rangle$, $z\langle 111 \rangle$. Likewise, for the {112} plane, the model orientation is $z\langle 110 \rangle$, $y\langle 112 \rangle$, and $z\langle 111 \rangle$. Finally, for the {123} plane, the crystal orientation is $x\langle 145 \rangle$, $y\langle 123 \rangle$, and $z\langle 111 \rangle$. Table 2 details the number of atoms and the number of atomic planes along the y direction for each plane.

30
31 Table 2: Number of atoms and number of atomic planes along the y direction for each plane.
32
33
34

Plane	No. of atoms	No. of planes
{110}	72	12
{112}	72	24
{123}	84	28

42 Each GSFE curve is computed by displacing the top half layers of atoms with respect
43 to the bottom half in the $z\langle 111 \rangle$ direction. Following each displacement, the top and bot-
44 tom atomic layers are held fixed, while the remaining layers are allowed to relax in the y
45 direction. Relaxation through energy minimization is achieved via the conjugate gradient
46 scheme. The minimization process is terminated when (i) the quotient of the change in
47 energy in successive iterations and the most recent energy magnitude is less than 10^{-12} or
48 (ii) when the global force vector length of all atoms is less than or equal to 10^{-12} eV/Å.
49
50
51
52
53
54
55
56
57
58
59
60
61
62
63
64
65

In addition to the GSFE curves, we also calculate the entire GSFE surfaces on the three slip planes in the four metals. The method is the same, except that the top half atomic layers are also displaced along the x direction, in addition to the z direction, to generate the entire energetic surface.

DFT calculations to date have only computed the GSFE curves in the $\langle 111 \rangle$ slip direction [16], not the entire GSFE surfaces for a given plane. As a consequence, for the comparisons between SNAP and DFT that follow, we focus on key properties of the GSFE curves, including the unstable stacking fault energy (USFE) γ_{usf} and the ideal shear strength T_{is} . They can be calculated from the GSFE curves γ_{gsf} via [11]:

$$\gamma_{\text{usf}} = \max[\gamma_{\text{gsf}}(d_z)] \quad (1)$$

$$T_{\text{is}} = \max\left[\frac{\partial \gamma_{\text{gsf}}(d_z)}{\partial d_z}\right] \quad (2)$$

3.2. Results and discussion

Figure 1 presents the calculated GSFE curves for all three planes in all four metals. The complete GSFE surfaces are provided in the Appendix. The MS calculation with SNAP generally produces higher GSF energies compared to DFT. The GSFE curves for Mo achieve the best agreement with DFT, especially for the $\{110\}$ plane, which only shows a 4% discrepancy in the peak value, the γ_{usf} . The results for Nb display the poorest agreement with DFT, where the largest discrepancy of 39% in the γ_{usf} is seen for the $\{112\}$ plane.

According to the hard-sphere model for the BCC lattice, the peak γ_{usf} in the $\{110\} \langle 111 \rangle$ GSFE curve should occur at a displacement of $b/2 = (a_0/4)\langle 111 \rangle$, indicating that the $\{110\}$ GSFE curve is symmetric [9]. In agreement, calculations from both SNAP and DFT on the $\{110\}$ planes exhibit symmetry for all four metals. By the same hard-sphere model, the displacement at γ_{usf} should be $b/3$ for the $\{112\}$ and $\{123\}$ higher order planes, making their GSFE curves asymmetric. While the DFT calculated curves exhibit this asymmetry,

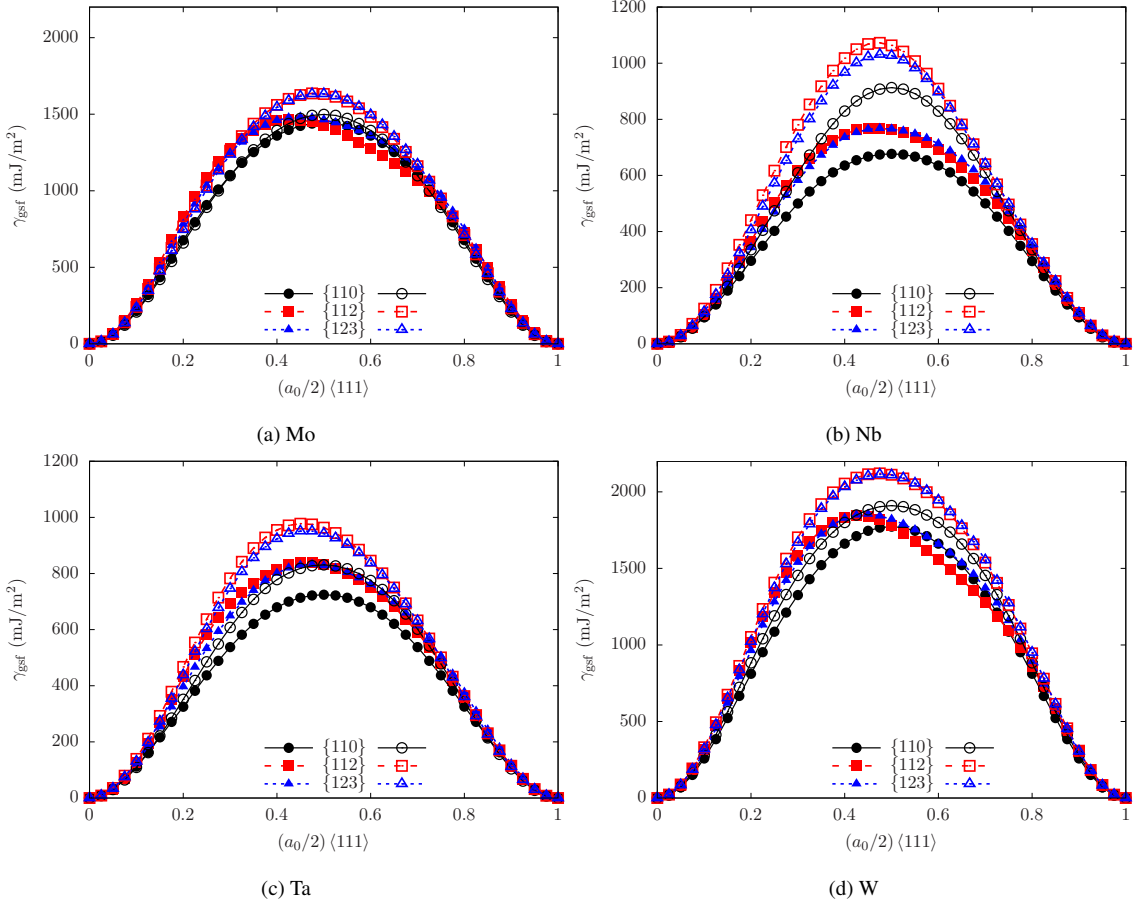


Figure 1: Relaxed GSFE curves on the three planes in four BCC refractory metals. SNAP-based results (open symbols) are compared with those from previous DFT calculations (filled symbols) from Ref. [16].

the SNAP calculated GSFE curves show a slightly lower degree of asymmetry. The closest result to DFT is realized with Ta, and the farthest one with W. Nonetheless, the prediction of asymmetry made by SNAP is an improvement from those provided by previous non-ML potentials. For instance, the calculated GSFE curves on the {112} and {123} planes of W with an EAM or an F-S potential are symmetric [25]. The fact that interatomic potentials show less or no degree of asymmetry suggests that that one fundamental cause for asymmetry could be quantum effects.

1
2
3
4
5
6 The γ_{usf} and T_{is} are compared in Table 3. Unlike γ_{usf} , T_{is} from SNAP lies within $\pm 10\%$
7 from that of DFT. Table 3 also compares the SNAP and DFT results with those from EAM
8 potentials (Mo [51], Nb [52], Ta [51], W [51]). In γ_{usf} , the EAM results are slightly closer
9 to DFT than SNAP; however, in T_{is} , SNAP results are clearly in most cases closer to DFT.
10
11
12
13

14 Results in Table 3 show that the group VI metals, Mo and W, have higher γ_{usf} and T_{is}
15 than the group V metals Nb and Ta. For the same plane, the metal with the highest γ_{usf}
16 among the four metals is W, with a value approximately twice that of Ta, which has the
17 lowest γ_{usf} , another feature in which SNAP and DFT agree.
18
19
20
21
22
23
24
25
26
27
28
29
30
31
32
33
34
35
36
37
38
39
40
41
42
43
44
45
46
47
48
49
50
51
52
53
54
55
56
57
58
59
60
61
62
63
64
65

Table 3: USFEs γ_{usf} (in mJ/m²) and ideal shear strengths T_{is} (in GPa). DFT results are from Ref. [16]. EAM potentials for Mo, Ta, and W are from Ref. [51], and that for Nb is from Ref. [52]. Note that EAM results for Mo and Nb have been reported in terms of γ_{usf} [49] and T_{is} [53].

Plane	Method	Mo	Nb	Ta	W	
{110}	γ_{usf}	SNAP	1498.8	912.94	830.8	1910.3
	γ_{usf}	DFT	1443.39	676.78	724.46	1772.74
	γ_{usf}	EAM	1458.05	604.87	751.11	1740.14
	T_{is}	SNAP	17.41	9.64	9.32	23.17
	T_{is}	DFT	17.7	7.51	7.78	20.99
	T_{is}	EAM	33.1	14.1	8.74	15.56
{112}	γ_{usf}	SNAP	1635.8	1072.7	977.64	2121
	γ_{usf}	DFT	1465.13	768.82	838.39	1845.83
	γ_{usf}	EAM	1689.03	697.23	868.3	2011.13
	T_{is}	SNAP	20.2	12.27	12.21	27.37
	T_{is}	DFT	21.67	9.88	11.4	26.46
	T_{is}	EAM	58.4	24.5	10.14	18.44
{123}	γ_{usf}	SNAP	1632.7	1031	950.93	2114.2
	γ_{usf}	DFT	1481.35	767.42	832.34	1854.3
	γ_{usf}	EAM	1657.93	684.71	852.26	1975.71
	T_{is}	SNAP	19.75	11.59	11.65	26.75
	T_{is}	DFT	20.35	8.91	9.97	24.99
	T_{is}	EAM	19.3	8.1	9.94	8.11

1
2
3
4
5
6
7
8
9
10
11
12
13
14
15
16
17
18
19
20
21
22
23
24
25
26
27
28
29
30
31
32
33
34
35
36
37
38
39
40
41
42
43
44
45
46
47
48
49
50
51
52
53
54
55
56
57
58
59
60
61
62
63
64
65

4. Peierls stress

4.1. Methodology

Table 4: The number of atoms, crystallographic orientations, and edge lengths for each simulation cell for Nb. The cells of other metals are the same in terms of number of atoms and crystallographic orientations, but the edge lengths are scaled with respect to their own lattice parameters.

Plane	Dislocation	No. of atoms	<i>x</i>	<i>y</i>	<i>z</i>	L_x (Å)	L_y (Å)	L_z (Å)
{110}	Edge	70308	[111]	[1̄10]	[11̄2]	401.8	395.1	8.1
	Screw	49980	[1̄12]	[1̄10]	[111]	399.2	399.8	5.8
{112}	Edge	80352	[111]	[1̄12]	[1̄10]	401.8	391.1	9.4
	Screw	49980	[1̄10]	[1̄12]	[111]	399.8	399.2	5.8
{123}	Edge	187488	[111]	[1̄23]	[5̄4̄1]	401.8	398.2	21.6
	Screw	51072	[5̄41]	[1̄23]	[111]	409.5	398.2	5.8

We employ the periodic array dislocation (PAD) model to calculate the Peierls stress [54]. Table 4 specifies the number of atoms, crystallographic orientations, and initial simulation cell edge lengths (L_x , L_y , L_z) of the simulation models. An edge or a screw dislocation with Burgers vector magnitude of $b = (a_0/2)\langle 111 \rangle$ is inserted into the center of the simulation cell by displacing atoms following linear elasticity theory [55–57]. The dislocation line is aligned with the z axis and the x - z plane corresponds to the slip plane, in which the dislocation lies. Periodic boundary conditions are applied in the x and z directions and traction-free boundary conditions are in the y direction [58]. Figure 2 shows the core structures of six dislocations in Nb.

An incremental strain tensor ϵ is applied by gradually applying a simple shear to the simulation cell. Each simulation cell starts as a cuboid and distorts to a triclinic shape with an increasing shear strain. The non-zero shear strain component for the screw dislocation case is ϵ_{yz} , while the non-zero component for the edge dislocation case is ϵ_{xy} .

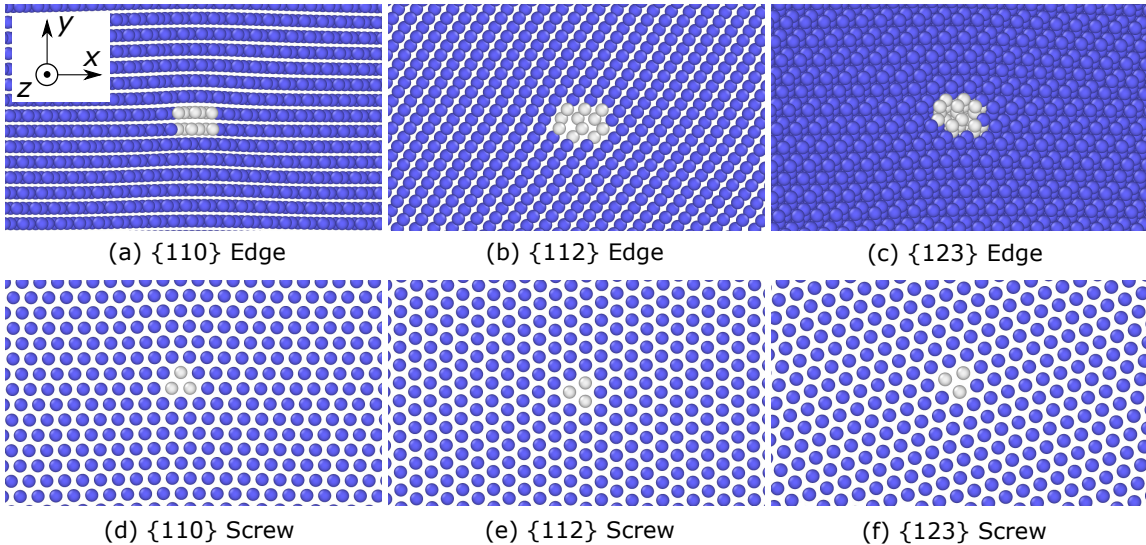


Figure 2: Atomistic structures of six dislocation cores in Nb, visualized in OVITO [59]. Atoms are colored by adaptive common neighbor analysis [60]: blue and white correspond to BCC and disordered local lattice structures, respectively.

All other strain components are zero. The strain increment at each step is 2×10^{-5} for edge dislocations and 2×10^{-6} for screw dislocations, until the maximum strain of 0.02 is reached.

Following each incremental strain, two minimization procedures are employed: the conjugate gradient algorithm and the fast inertial relaxation engine method [61]. The minimization stops when either of the conditions stated earlier in the GSFE calculations in Section 3.1 is met. The Peierls stress is then identified as the minimum stress at which the dislocation starts to move. In all planes, we carry out separate simulations for shearing in the positive (given in Table 4) and negative directions to assess the slip asymmetry in the Peierls stress. We refer to positive shearing as “forward”, and negative shearing as “backward”. For the {112} plane only, the backward sense we assigned is commonly known as the anti-twinning direction, while the forward one the twinning direction [62].

1
2
3
4
5
6 Before embarking on systematic atomistic simulations in the four refractories, we con-
7 duct a study on the effects of the simulation cell size on the Peierls stress value. For this,
8 we choose Nb with an edge dislocation on the {112} plane and apply the shear strain in the
9 twinning direction. For the effect of dislocation line length, L_x and L_y are fixed, while L_z
10 is varied from 4.7, 9.4, 14.1, to 18.8 Å. For the effect of the other two edge lengths, a fixed
11 dislocation line length ($L_z = 9.4$ Å) is chosen, while $L_x \times L_y$ is varied from 301.0×293.3 Å²,
12 401.8 × 391.1 Å², to 502.6 × 488.8 Å². It is shown that in general the Peierls stress increases
13 as L_z decreases or as L_x and L_y increase. Note that a recent study on the same dislocation
14 in Nb using an EAM potential [52] or an F-S potential [63] showed that the effect of L_x
15 and L_y on the Peierls stress value depends on the interatomic potential [64], hence justifying
16 the need to identify these dimensions for SNAP. Overall, the resulting Peierls stresses
17 here do not show a strong correlation with the simulation cell size. With changing L_z , the
18 Peierls stress varies within ±2%, and with varying L_x and L_y , it varies within ±8%. In all
19 subsequent simulations, we employ the simulation cell sizes given in Table 4 for Nb and
20 simulation cell sizes with similar scaling with lattice parameters for the other three metals.
21
22
23
24
25
26
27
28
29
30
31
32
33
34
35
36

4.2. Results and discussion

37
38 In this section, the MS results using SNAP are compared with those from previous
39 MS simulations, near 0 K MD simulations, *ab initio* calculations, and experiments. We
40 exclude estimates of Peierls stress calculated from the GSFE curve, e.g., Ref. [13, 65].
41 The number of different potentials used previously is large, including the F-S, EAM, mod-
42 ified embedded-atom method (MEAM), bond-order potential (BOP), modified general-
43 ized pseudo potential theory (MGPT), first-principles-based embedded atom model force
44 field (qEAM-FF), and the angular dependent potential (ADP). The *ab initio* calculations
45 used are either DFT or the tight-binding (TB) method. The TB calculations used the
46 environment-dependent tight-binding (EDTB) potential, while the DFT calculations em-
47
48
49
50
51
52
53
54
55
56

ployed the projector augmented wave (PAW) method, ultrasoft pseudopotential (USPP), and norm-conserving pseudopotential (NCP).

In addition to the interatomic potential, prior MD and MS works used different initial dislocation configurations for calculating the Peierls stress. As mentioned, for most of the SNAP Peierls stress calculations here, we use the PAD configuration. Apart from PAD, six other model configurations have been adopted in the literature, namely the fixed boundary circle (FBC), fixed boundary square (FBS), horizontal dipole (dipole-H), vertical dipole (dipole-V), quadrupole, and Green's function boundary condition (GFBC) models. In a recent study, the Peierls stresses for an edge dislocation on the {112} plane in Nb calculated using PAD and the first five aforementioned models were compared [64]. It was found that even with the same interatomic potential, cell size, material, and dislocation character, these six configurations produce significantly different Peierls stresses. In addition, only the Peierls stress from the PAD model converged to a single value as the simulation cell increased. In this work, at the end of the discussion, for the screw dislocation in Ta and W, we compare the SNAP Peierls stress from six model configurations.

4.2.1. Peierls stress of edge dislocations

Table 5 summarizes the calculated Peierls stresses for edge dislocations. In all cases, the dislocation glides on the habit plane. For comparison, Table 5 also lists edge dislocation Peierls stresses previously calculated with atomistic simulation, involving other interatomic potentials and/or other model configurations. To the best of our knowledge, neither *ab initio* calculations nor measured values for the Peierls stresses of edge dislocations in any of these metals have been previously reported.

Considering all Peierls stresses computed to date shows substantial variation among them. Li *et al* [66] used the same ML SNAP to calculate the Peierls stresses on the {110} plane in all four metals but in near 0 K MD simulations. For Nb and Ta, their values are

close to ours, within 20 MPa, but for Mo and W, there exist larger differences. In general, discrepancies can be attributed to the choice of cell size and model configuration. They used the FBC model configuration and a smaller cell size of 20 nm diameter compared to the approximately 40 nm size used in the current PAD configuration. The remaining prior atomistic simulation studies used the MS method and non-ML interatomic potentials. For all three planes in Nb and Mo, the SNAP results are higher by approximately 93% than the Peierls stresses recently calculated using EAM potentials [53]. The Peierls stress on the {112} plane calculated for Mo using an MEAM potential [67] is much smaller, by 89% compared to the value of this study. Jian *et al* [64] computed Peierls stresses of Nb in both twinning and anti-twinning directions on the {112} plane using an EAM [52] and an F-S potential [63]. Using the same loading mode, model configuration, and a similar cell size as here, their results when using EAM are higher by 330% than ours but when using F-S, they are lower than ours. In Ta, another calculation on the {110} plane using an F-S potential [63] was reported in Ref. [68] and the value obtained is comparable to the one we obtain here with SNAP.

Our results show that for all four refractory metals, the Peierls stresses for edge dislocations on the {110} and {123} planes are relatively low compared to those on the {112} plane. The highest Peierls stress is for W in the {112} plane with 2276 MPa in the forward direction. In addition, no metal consistently achieves the highest or lowest Peierls stress for all planes. For example, Mo achieves the highest Peierls stress on the {110} plane and W the highest on the {112} and {123} planes. The Peierls stresses are the lowest for Ta on the {123} plane, and for W on the {110} plane.

Table 5: Peierls stress values (in MPa) for edge dislocations on different slip planes in four BCC metals. All used MS simulations except [66], which used near 0 K MD simulations. Data from [64] were taken for comparable sizes (edge length or diameter per dislocation \approx 50 nm) and the same shear-controlled loading as the present work. T: twinning; AT: anti-twinning; fw: forward; bw: backward.

Metal	Model	Potential	$\{110\}_{fw}$	$\{110\}_{bw}$	$\{112\}_{fw}$ (T)	$\{112\}_{bw}$ (AT)	$\{123\}_{fw}$	$\{123\}_{bw}$
Mo	PAD	SNAP [66]	138	134	1037	710	231	208
Mo [66]	FBC	SNAP [66]	76	-	-	-	-	-
Mo [53]	PAD	EAM [51]	50	50	533	734	160	117
Mo [67]	FBC	MEAM [67]	-	-	150	-	-	-
Nb	PAD	SNAP [66]	23	25	282	316	31	85
Nb [66]	FBC	SNAP [66]	29	-	-	-	-	-
Nb [53]	PAD	EAM [52]	6	6	118	99	12	13
Nb [64]	FBC	EAM [63]	-	-	509	577	-	-
Nb [64]	FBS	EAM [63]	-	-	493	574	-	-
Nb [64]	PAD	EAM [63]	-	-	504	549	-	-
Nb [64]	Dipole-H	EAM [63]	-	-	517	567	-	-
Nb [64]	Dipole-V	EAM [63]	-	-	516	567	-	-
Nb [64]	Quadrupole	EAM [63]	-	-	524	566	-	-
Nb [64]	FBC	EAM [52]	-	-	97	121	-	-
Nb [64]	FBS	EAM [52]	-	-	102	129	-	-
Nb [64]	PAD	EAM [52]	-	-	105	94	-	-
Nb [64]	Dipole-V	EAM [52]	-	-	119	99	-	-
Nb [64]	Quadrupole	EAM [52]	-	-	121	101	-	-
Ta	PAD	SNAP [66]	20	21	162	172	4	4
Ta [66]	FBC	SNAP [66]	41	-	-	-	-	-
Ta [68]	FBS	F-S [63]	30	-	-	-	-	-
W	PAD	SNAP [66]	8	7	2276	1042	736	213
W [66]	FBC	SNAP [66]	56	-	-	-	-	-

1
2
3
4
5
6 *4.2.2. Peierls stress or CRSS of screw dislocations*

7 Table 6: Peierls stress or CRSS (in MPa) for screw dislocations on different slip planes in Mo.

Method	Model	Potential	$\{110\}_{fw}$	$\{110\}_{bw}$	$\{112\}_{fw}$ (T)	$\{112\}_{bw}$ (AT)	$\{123\}_{fw}$	$\{123\}_{bw}$
MS	PAD	SNAP [66]	4054	4054	4317*	5510*	3932*	4808*
MS [69]	Quadrupole	F-S [63]	2400	-	-	-	-	-
MS [53]	PAD	EAM [51]	-	-	2496	3842	-	-
MS [67]	FBC	MEAM [67]	1790	-	2020	2360	-	-
MS [70]	FBC	BOP [70]	2600	-	2800	3500	-	-
MS [71]	GFBC	MGPT [71]	866	-	1235	1876	-	-
MS [72]	GFBC	MGPT [73]	2610	-	2340	7290	-	-
MS [74]	FBS	MGPT [73]	-	-	3440*	-	-	-
MS [75]	FBS	MGPT [73]	6192	-	3440*	-	-	-
MS [71]	FBC	F-S [63]	2354	-	2372	4199	-	-
MS [76]	FBS	F-S [63]	3510	-	3510	5990	-	-
MD [66]	FBC	SNAP [66]	1376	-	-	-	-	-
TB [69]	Quadrupole	EDTB [77]	3800	-	-	-	-	-
DFT [30]	Quadrupole	USPP [78]	1800	-	-	-	-	-
DFT [28]	GFBC	USPP [78]	2085	-	1740	3480	-	-
DFT [32]	Quadrupole	USPP [78]	1350	-	-	-	-	-
DFT [31]	Quadrupole	PAW [79]	1600	-	-	-	-	-
DFT [29]	GFBC	USPP [78]	2420	-	1738	3173	-	-
Exp [80]			870	-	690	-	-	-
Exp [81]			730	-	-	-	-	-

52 Tables 6–9 present the Peierls stresses for screw dislocations in the four metals calcu-
53 lated here and by simulation or measured in experiments from other studies. Since screw
54

character dislocations can cross slip, the screw dislocation may not necessarily glide on its habit plane when the deformation is applied. This behavior has been studied in detail in Ref. [82] and was attributed to the incorrect dislocation core structures rendered by the interatomic potentials. Here, in some metals and glide planes, we find that the dislocation glides on its habit plane, while in others it cross slips onto another plane. When it remains on its habit plane, the critical stress to move the dislocation is the Peierls stress. However, should it cross slip and glide on another plane, we refer to this motion as unstable and the critical stress for first motion as a critical resolved shear stress (CRSS) instead of a Peierls stress. In Tables 6–9, all CRSSes are marked with *. In a few studies, the critical stresses were not reported when the screw dislocation cross slipped off-plane [53]. In other works, when the critical stress was reported but not whether the dislocation actually moved on the intended plane, the critical stress is referred to as a Peierls stress. Since the Peierls stress on the {110} plane is expected to be symmetric, most prior studies did not specify the direction for which the Peierls stress is computed. Although their true directions are unknown, all Peierls stress calculated on the {110} plane previously are listed under our forward direction in Table 4.

In Table 6, for Mo, the SNAP Peierls stresses are higher in the {110} and {112} glide planes compared to those using other interatomic potentials, from experiments, and from DFT. For the {110} plane, DFT calculations and experiments reported values in the range of 1350–2420 MPa, while previous MS and TB results ranged from 866–6192 MPa. Our result is 4054 MPa. This value is on average 1.54 times larger than those from non-ML interatomic potentials. It is more than twice the value obtained by Li *et al* [66] using SNAP. As mentioned earlier, differences may arise from differences in the model size and model configuration used (PAD here vs. FBC there). We adopt a size that is two times larger and known to produce size insensitive Peierls stress values when using PAD [64].

For Nb, the Peierls stress on the {110} plane by SNAP (840 MPa) is very close to those

Table 7: Peierls stress or CRSS (in MPa) of screw dislocations on different slip planes in Nb.

Method	Model	Potential	$\{110\}_{fw}$	$\{110\}_{bw}$	$\{112\}_{fw}$ (T)	$\{112\}_{bw}$ (AT)	$\{123\}_{fw}$	$\{123\}_{bw}$
MS	PAD	SNAP [66]	840	827*	1452*	2106*	1177*	568*
MS [83]	FBC	EAM [83]	1313*	-	1130	3844	-	-
MS [53]	PAD	EAM [52]	-	-	859	-	-	-
MS [64]	FBC	EAM [83]	-	-	1264	-	-	-
MD [66]	FBC	SNAP [66]	889	-	-	-	-	-
DFT [31]	Quadrupole	PAW [79]	740	-	-	-	-	-
DFT [33]	Quadrupole	USPP [78]	650–860	-	-	-	-	-
Exp [84]			415	-	-	-	-	-

from DFT reported in the literature (650–860 MPa) [31, 33] and is much lower than the CRSS predicted by an EAM potential (1313 MPa) [83]. In the SNAP calculation, the screw dislocation glides stably on the $\{110\}$ plane, whereas in the EAM calculation it does not. However, the opposite is true for the $\{112\}$ plane, where the screw dislocation cross slips away from the $\{112\}$ plane in Nb by SNAP, whereas it glides stably by the two EAM potentials [52, 83]. No DFT results on the $\{112\}$ plane exist for Nb.

In Table 8, prior atomistic simulations for the $\{110\}$ plane in Ta obtained Peierls stresses, ranging from 655–5916 MPa and DFT results yielding 810–1760 MPa. Our SNAP-based CRSS value is 956 MPa, which is much closer to those based on DFT than those predicted by non-ML interatomic potentials.

In W, on the $\{110\}$ plane, our SNAP-based Peierls stress is 3773 MPa, while DFT data range from 1800 to 2850 MPa. To the best of our knowledge, no non-ML potential has been applied to calculate the Peierls stress in W, for either an edge or screw dislocation, on any of the three planes studied here.

Experimentally measured Peierls stresses in BCC metals are provided in the last rows

Table 8: Peierls stress or CRSS (in MPa) of screw dislocations on different slip planes in Ta.

Method	Model	Potential	$\{110\}_{fw}$	$\{110\}_{bw}$	$\{112\}_{fw}$ (T)	$\{112\}_{bw}$ (AT)	$\{123\}_{fw}$	$\{123\}_{bw}$
MS	PAD	SNAP [66]	956*	956*	893*	3583*	845*	2123*
MS [68]	FBS	F-S [63]	2785	-	-	-	-	-
MS [85]	FBC	qEAM-FF [86]	740	-	-	-	-	-
MS [76]	FBS	F-S [63]	5916	-	4120	14832	-	-
MS [71]	FBC	F-S [63]	3060*	-	2149	-	-	-
MS [75]	FBS	MGPT [20]	1875	-	1375*	-	-	-
MS [20]	GFBC	MGPT [20]	640*	-	605	1400	-	-
MS [82]	FBS	F-S [63]	2864*	-	2033	7207	-	-
MS [82]	FBS	EAM [87]	2023	-	2320	8624*	-	-
MS [82]	FBS	EAM [88]	5698*	-	3634	9416	-	-
MS [82]	FBS	EAM [89]	3357*	-	2012	8357*	-	-
MS [82]	FBS	ADP [90]	1242*	-	842	4086*	-	-
MD [66]	FBC	SNAP [66]	912	-	-	-	-	-
MD [91]	Dipole-H	qEAM-FF [86]	1800	-	-	-	-	-
MD [92]	Dipole-H	qEAM-FF [86]	-	-	790	1430	-	-
MD [34]	Quadrupole	qEAM-FF [86]	655	-	575	1075	-	-
DFT [34]	Quadrupole	NCPP [93]	1410–1760	-	-	-	-	-
DFT [29]	GFBC	USPP [78]	1550	-	701	3591	-	-
DFT [31]	Quadrupole	PAW [79]	860	-	-	-	-	-
DFT [33]	Quadrupole	USPP [78]	810–920	-	-	-	-	-
Exp [94]			340	-	-	-	-	-

of Tables 6–9. For Peierls stress calculations, screw dislocations on the $\{110\}$ plane is the most commonly studied dislocation in the literature. For the $\{112\}$ plane, no experimen-

Table 9: Peierls stress or CRSS (in MPa) of screw dislocations on different slip planes in W.

Method	Model	Potential	$\{110\}_{fw}$	$\{110\}_{bw}$	$\{112\}_{fw}$ (T)	$\{112\}_{bw}$ (AT)	$\{123\}_{fw}$	$\{123\}_{bw}$
MS	PAD	SNAP [66]	3773	3772	3958*	5937	3689	4569*
MD [66]	FBC	SNAP [66]	1686	-	-	-	-	-
DFT [22]	Quadrupole	PAW [79]	2850	-	-	-	-	-
DFT [31]	Quadrupole	PAW [79]	2400	-	-	-	-	-
DFT [32]	Quadrupole	USPP [78]	1970	-	-	-	-	-
DFT [33]	Quadrupole	USPP [78]	1800	-	-	-	-	-
Exp [95]			960	-	-	-	-	-

tal results for screw dislocations have been previously reported. Calculations of Peierls stresses are quantitatively and consistently off from measurement. Measurements are typically much lower than any of the calculated Peierls stresses and they are even lower than the DFT data in all four metals. On the one hand, it can be concluded that atomistic calculations using interatomic potentials can be useful in providing trends and relative values of dislocation resistance, but not precise values. But on the other hand, it has been suggested that the low Peierls stresses for screw dislocations from experiments could be misleading due to possible internal stress concentrations that reduced the energy barrier for kink nucleation [67, 96, 97].

4.2.3. Effect of model configuration for screw dislocations

As mentioned, a recent work studied the effects of the model configuration on the Peierls stress values of an edge dislocation on the $\{112\}$ plane in Nb [64]. Screw dislocations, however, were not studied there, and since edge dislocations glide stably on the habit plane, the question remains whether the model configuration can also affect the stability of screw dislocation glide.

Table 10: Peierls stress or CRSS (in MPa) of a screw dislocation on the {112} plane in Ta and W based on different model configurations.

Metal	Direction	PAD	FBC	FBS	Dipole-H	Dipole-V	Quadrupole
Ta	Twinning	893*	973*	990*	948*	925*	936*
	Anti-twinning	3583*	3700	3643	3481*	3582	3618
W	Twinning	3958*	4046	4029	4081*	4002*	3991
	Anti-twinning	5937	6050	5980	5918	5975	5975

To address this question, we examine the effect of model configuration on the glide of {112} screw dislocations in Ta and W. We consider five additional models apart from PAD: FBC, FBS, dipole-H, dipole-V, and quadrupole. Results presented in Table 10 find that the model configuration has a strong effect on the plane on which the screw dislocation ultimately glides. In Ta, the twinning direction glide is unstable in all models. The anti-twinning glide is also unstable when using the PAD and dipole-H model configurations, but stable when the other four model configurations are used. In W, anti-twinning direction glide on the {112} plane is stable for all model configurations. The twinning direction, however, is unstable in the PAD, dipole-H, and dipole-V configurations, but stable in the other three. For the same metal, the Peierls stress values obtained under stable glide from the different configurations are close, lying within 1.8%, while the CRSS values obtained when the dislocation cross slips to another plane deviates slightly more, by 5.4%. Model configurations that support stable glide can yield consistent values, provided that all else is equal.

4.2.4. Anisotropy in critical stress

The degree of slip-plane anisotropy can be measured by calculating the coefficient of variation (CoV) in Peierls stresses or CRSS among all distinct planes belonging to

Table 11: CoV in Peierls stress or CRSS across all planes for each dislocation in each BCC metal. Results are based on MS simulations in this paper using SNAP, as presented in Tables 5–9.

	Mo	Nb	Ta	W
Edge	0.839	1.025	1.25	1.116
Screw	0.125	0.437	0.646	0.186

each metal [53]. For each dislocation, the CoV is calculated as the standard deviation divided by the mean among the six cases (three slip planes, for each of which there are two shearing directions). The CoVs of the four metals are summarized in Table 11. For the edge dislocation, the four metals exhibit a similar degree of slip-plane anisotropy in the Peierls stress. These values are close to those from a recent MS study for these four slip planes using EAM potentials: 1.13 for Mo and 1.31 for Nb [53]. On the other hand, screw dislocations possess smaller CoVs in Peierls stress or CRSS than edge dislocations, indicating that their critical stress values are more uniform across different slip planes. For both dislocations, CoV is the highest in Ta and the lowest in Mo.

Another measure of stress anisotropy is glide asymmetry, the difference between the Peierls stress or CRSS in the forward and backward slip directions. Table 12 summarizes the glide asymmetry ratios. About the glide direction (i.e., x axis), the atomic structure of the $\{110\}$ plane is symmetric (see Figure 2(a,d)), and based on this geometric argument alone, the Peierls stress is expected to be equal in the forward and backward direction. The calculated Peierls stresses in the $\{110\}$ plane exhibit near glide symmetry, with ratios ranging from 0.875–1.05. Despite this, in some cases, the motion of the screw dislocation is not necessarily symmetric. In Ta and Nb, for instance, the dislocation cross slips onto another $\{110\}$ plane when sheared in one direction but glides on the habit plane in the other.

For the $\{112\}$ plane, glide asymmetry is expected for screw dislocations. Our results

Table 12: Backward-to-forward ratios in the Peierls stresses or CRSS on three slip planes in four BCC metals. Results are based on MS simulations in this paper using SNAP, as presented in Tables 5–9.

Metal	Dislocation	{110}	{112}	{123}
Mo	Edge	0.971	0.685	0.9
	Screw	1	1.276	1.223
Nb	Edge	1.087	1.121	2.742
	Screw	0.985	1.45	0.483
Ta	Edge	1.05	1.062	1
	Screw	1	4.012	2.512
W	Edge	0.875	0.458	0.289
	Screw	1	1.5	1.239

indicate glide asymmetry in all cases. For the screw dislocations, the Peierls stress or CRSS in the anti-twinning (AT) direction is always higher than that in the twinning (T) direction on all slip planes in all four metals, where the AT/T ratios range around 1.28–4.01. These ratios are similar to the range 1.170–4.85 from MS and 1.83–5.12 from DFT calculations (see Tables 5–9). For edge dislocations, the glide asymmetry is not consistent as it is for screw dislocations. SNAP predicts that the AT Peierls stress is higher than the twinning one in Nb and Ta, but reversed in Mo and W. Evaluation of computed Peierls stress for edge dislocations from other studies also finds that the AT/T asymmetry depends on the material, interatomic potential, and model configuration [53, 64].

Like the {112} plane, the {123} plane exhibits similar glide asymmetry, where the ratio of Peierls stresses in the two opposing senses of slip is 0.29–2.74. Unlike the {112} plane, however, the {123} plane has no association with twinning. For most metals except Nb, the forward slip direction on the {123} plane has a lower Peierls stress than that in the backward direction.

Table 13: Screw-to-edge ratios in the Peierls stress or CRSS on different slip planes in four BCC metals.
 Results are based on MS simulations in this paper using SNAP, as presented in Tables 5–9.

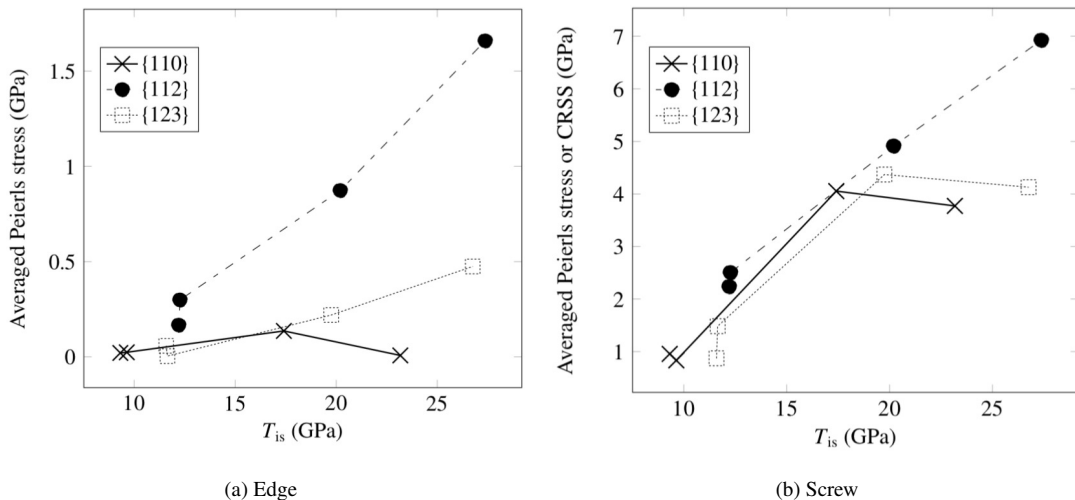
Metal	$\{110\}_{fw}$	$\{110\}_{bw}$	$\{112\}_{fw}$ (T)	$\{112\}_{bw}$ (AT)	$\{123\}_{fw}$	$\{123\}_{bw}$
Mo	29.38	30.25	4.16	7.76	17.02	23.12
Nb	36.52	33.08	5.15	6.66	37.97	6.68
Ta	47.8	40.52	5.51	20.83	211.25	530.75
W	471.63	538.85	1.74	5.7	5.01	21.45

The last measure of the anisotropy in critical stresses is the screw-to-edge ratio in the Peierls stress or CRSS along the same shear direction on the same slip plane. It is conventionally known that plasticity of BCC metals at low temperatures is controlled by the glide of screw dislocations since the Peierls stress and Peierls barrier are one to two orders of magnitude higher for screw dislocations than for edge dislocations [98, 99]. In agreement, Peierls stresses for edge dislocations calculated here are much smaller than those of screw dislocations. Screw-to-edge ratios in the Peierls stress or CRSS on different slip planes in four BCC metals are summarized in Table 13. It is shown that the ratios are generally high on the $\{110\}$ plane, with the highest one being 539 for the backward direction in W. In some other cases, such as in the higher order $\{112\}$ and $\{123\}$ planes in Mo and W, the screw-to-edge ratios in the critical stress are remarkably much smaller, being in the range of 1.74–23.12. For W on the $\{112\}$ plane, for instance, the ratio is only 1.74. Clearly with such low ratios, the effects of edge dislocation glide on plasticity cannot be considered negligible on these slip planes.

1
2
3
4
5
6 4.2.5. Correlation between ideal shear strength and Peierls stress
7
8
9

10 Table 14: Averaged Peierls stresses or CRSS (in MPa) on three slip planes in four BCC metals. Results are
11 based on MS simulations in this paper using SNAP, as presented in Tables 5–9.

Metal	Dislocation	{110}	{112}	{123}
Mo	Edge	136	873.5	219.5
	Screw	4054	4913.5	4370
Nb	Edge	24	299	58
	Screw	833.5	1779	872.5
Ta	Edge	20.5	167	4
	Screw	956	2238	1484
W	Edge	7.5	1659	474.5
	Screw	3772.5	4947.5	4129



49 Figure 3: Averaged Peierls stress or CRSS vs. ideal shear strength T_{is} for (a) edge and (b) screw dislocations
50 across different slip planes in the four metals. The lines drawn between symbols are intended to only guide
51 the eye.
52
53
54
55
56
57
58
59
60
61
62
63
64
65

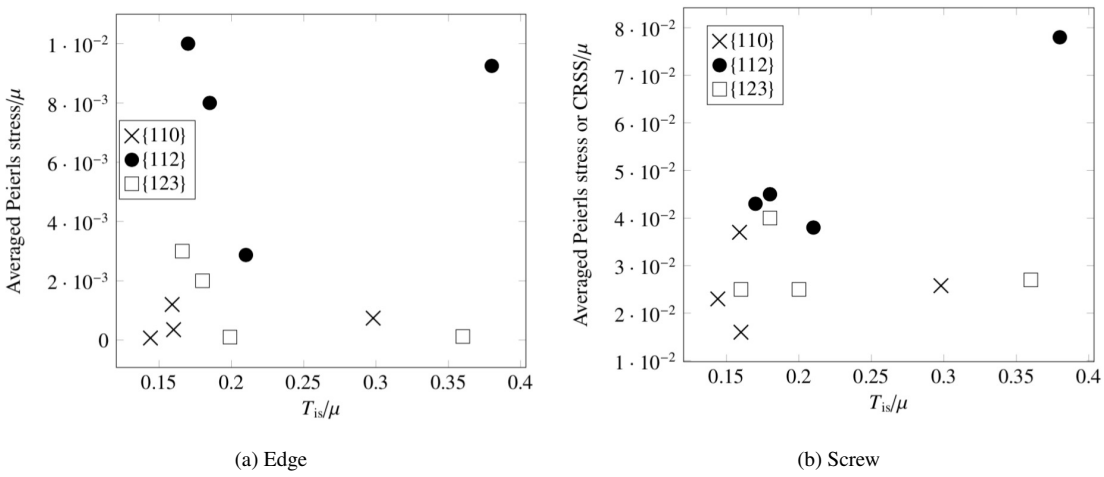


Figure 4: Normalized averaged Peierls stress or CRSS/μ vs. normalized ideal shear strength T_{is}/μ for (a) edge and (b) screw dislocations across different slip planes in the four metals, where μ is the isotropic shear modulus in Hill form presented in Table 1.

As mentioned in section 1, there are two measures of glide resistance that can be obtained from atomistic simulations, the Peierls stress of a dislocation and the ideal shear strength T_{is} (Equation 2). For the same plane, the averaged Peierls stress or CRSS between the forward and backward directions are calculated and presented in Table 14. Figure 3 presents the averaged Peierls stress or CRSS versus T_{is} , indicating a positive correlation with the exception of edge dislocations on the {110} plane. The Peierls stress or CRSS on the higher order {112} and {123} planes are higher than that on the {110} plane in the same metal, just as the higher order planes possess higher T_{is} than the {110} plane. Experimental studies obtained similar ranking among the screw dislocations for the {110} plane. Specifically, the Peierls stresses for Mo and W are higher than those for Nb and Ta, with 730–870 MPa for Mo [80, 81] and 960 MPa for W [95], as opposed to 415 MPa for Nb [84] and 340 MPa [94] for Ta. However, when the critical stresses are normalized by their corresponding shear modulus, no correlation is observed, see Figure 4. This effect

of normalization means that metals with high Peierls stresses or CRSS and T_{is} have a proportionally much higher shear modulus than metals with smaller critical stresses. From a physical viewpoint, the uncorrelatedness may not be surprising since Peierls stresses in BCC metals are known to not only depend on bonding across the plane but also on the atomic structure of the dislocation core [100, 101], which is missing in the GSFE calculation.

1
2
3
4
5
6 **5. Conclusions**
7

8
9 In this work, the GSFE curves and Peierls stress of four BCC refractory metals (Mo,
10 Nb, Ta, W) are calculated using a recently developed ML-based interatomic potential
11 called SNAP. The calculations focus on both screw and edge character dislocations on
12 three common glide planes {110}, {112}, and {123}. On all three planes, the GSFE curves
13 from SNAP agree well with those from DFT and when compared to non-ML interatomic
14 potentials, are more accurate in calculations of the ideal shear strength. The SNAP-
15 calculated GSFE curves on the higher order planes show lower degrees of asymmetry
16 than the DFT curves. This can be regarded as an improvement from those calculated by
17 other interatomic potentials, which produce symmetric curves for these planes. The fact
18 that SNAP and other interatomic potentials give rise to less or no asymmetry suggests that
19 quantum effects may be responsible.
20
21

22 We show that SNAP provides screw dislocation Peierls stresses close to those of DFT,
23 much closer than those achieved by non-ML potentials. Like DFT, the values are still
24 higher than those from the few experimentally measured values in the literature. For all
25 metals, the edge dislocation Peierls stress are the lowest on the {110} plane and the highest
26 on the {112} plane. For screw dislocations, glide on either the {110} or {123} plane is the
27 easiest. Both the {112} and {123} planes exhibit glide asymmetry, being on average 1.9
28 times higher in one direction than the other. The screw-to-edge ratio is large, in the range
29 of $\approx 29\text{--}539$ for the {110} plane, but substantially smaller, in the range of $\approx 2\text{--}21$, for the
30 {112} plane. The slip-plane anisotropy, the difference in the Peierls stresses among the
31 three distinct crystallographic planes, is the greatest for Ta and minimal for Mo, for both
32 edge and screw dislocations. Last, we observed that in most cases, the screw dislocation
33 cross slips away from the habit plane, and this outcome can change depending on the
34 model configuration used, i.e., PAD, FBC, FBS, dipole-H, dipole-V, or quadrupole.
35
36
37
38
39
40
41
42
43
44
45
46
47
48
49
50
51
52
53
54
55
56
57
58
59
60
61
62
63
64
65

1
2
3
4
5
6 **Data availability**
7

8
9 The raw/processed data required to reproduce these findings cannot be shared at this
10 time as the data also forms part of an ongoing study.
11
12

13
14 **Acknowledgements**
15

16
17 XW would like to thank Yuanchao Hu for helpful discussions on using LAMMPS.
18 WJ and IJB would like to acknowledge funding from the Office of Naval Research under
19 Grant No. N000141712810. SX and IJB gratefully acknowledge support from the Office
20 of Naval Research under contract ONR BRC Grant N00014-18-1-2392. Use was made
21 of computational facilities purchased with funds from the National Science Foundation
22 (CNS1725797) and administered by the Center for Scientific Computing (CSC). The CSC
23 is supported by the CNSI and the Materials Research Science and Engineering Center
24 (MRSEC; NSF DMR 1720256) at UC Santa Barbara.
25
26
27
28
29
30
31
32
33
34
35
36
37
38
39
40
41
42
43
44
45
46
47
48
49
50
51
52
53
54
55
56
57
58
59
60
61
62
63
64
65

1
2
3
4
5
6
7
8
9
10
11
12
13
14
15
16
17
18
19
20
21
22
23
24
25
26
27
28
29
30
31
32
33
34
35
36
37
38
39
40
41
42
43
44
45
46
47
48
49
50
51
52
53
54
55
56
57
58
59
60
61
62
63
64
65

Appendix A. GSFE surfaces

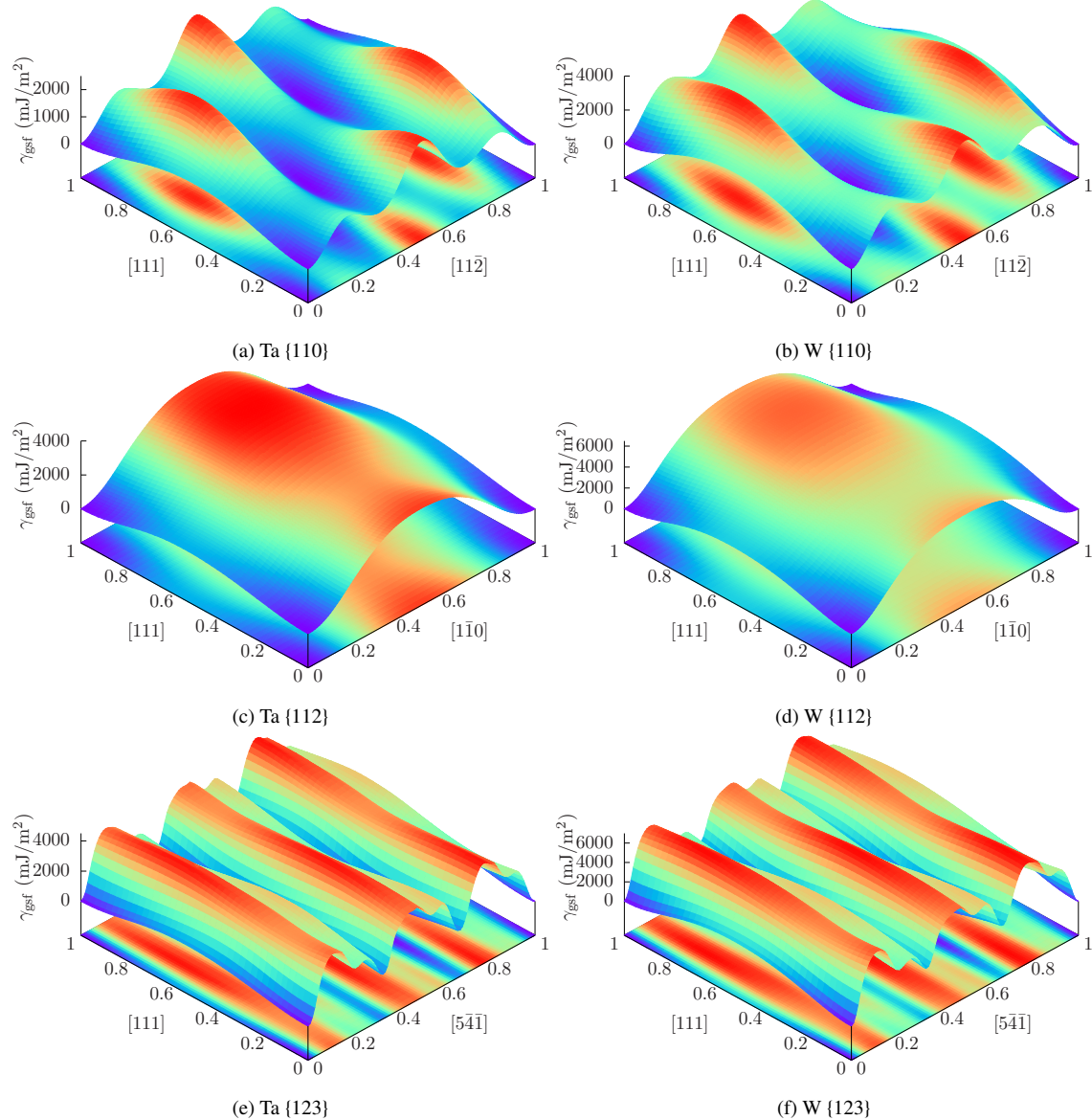


Figure A.1: Relaxed GSFE surfaces on {110}, {112}, and {123} planes in Ta and W, based on SNAP [66].

1
2
3
4
5
6
7

References

- 8
9 [1] T. E. Tietz, J. W. Wilson, Behavior and properties of refractory metals, Stanford
10 University Press, 1965.
11
12
13 [2] S. Xu, Modelling plastic deformation of nano/submicron-sized tungsten pillars un-
14 der compression: A coarse-grained atomistic approach, *Int. J. Multiscale Comput.*
15 *Eng.* 16 (2018) 367–376. URL: <http://www.dl.begellhouse.com/journals/61fd1b191cf7e96f,77bb56c9113fd8ad,519a0e1634b8eddd.html>.
16 doi:10.1615/IntJMultCompEng.2018026027.
17
18
19 [3] T. Trusty, S. Xu, I. J. Beyerlein, Atomistic simulations of tungsten nanotubes under
20 uniform tensile loading, *J. Appl. Phys.* 126 (2019) 095105. URL: <https://aip.scitation.org/doi/full/10.1063/1.5110167>. doi:10.1063/1.5110167.
21
22
23 [4] F. Wang, G. H. Balbus, S. Xu, Y. Su, J. Shin, P. F. Rottmann, K. E. Knippling,
24 J.-C. Stinville, L. H. Mills, O. N. Senkov, I. J. Beyerlein, T. M. Pollock, D. S.
25 Gianola, Multiplicity of dislocation pathways in a refractory multiprincipal element
26 alloy, *Science* 370 (2020) 95–101. URL: <https://science.sciencemag.org/content/370/6512/95>. doi:10.1126/science.aba3722.
27
28
29 [5] K. Maier, M. Peo, B. Saile, H. Schaefer, A. Seeger, High-temperature positron
30 annihilation and vacancy formation in refractory metals, *Philos. Mag. A* 40 (1979)
31 701–728.
32
33
34 [6] V. S. Prasad, R. Baligidad, A. A. Gokhale, Niobium and other high temperature
35 refractory metals for aerospace applications, in: *Aerospace Materials and Material*
36 *Technologies*, Springer, 2017, pp. 267–288.
37
38
39
40
41
42
43
44
45
46
47
48
49
50
51
52
53
54
55
56
57
58
59
60
61
62
63
64
65

- 1
2
3
4
5
6 [7] D. Inman, S. H. White, The production of refractory metals by the electrol-
7
8
9
10
11
12
13
14
15
16
17
18
19
20
21
22
23
24
25
26
27
28
29
30
31
32
33
34
35
36
37
38
39
40
41
42
43
44
45
46
47
48
49
50
51
52
53
54
55
56
57
58
59
60
61
62
63
64
65
- [7] D. Inman, S. H. White, The production of refractory metals by the electrolysis of molten salts; design factors and limitations, *J. Appl. Electrochem.* 8 (1978) 375–390. URL: <https://doi.org/10.1007/BF00615833>. doi:10.1007/BF00615833.
- [8] S. Xu, S. Z. Chavoshi, Y. Su, Deformation mechanisms in nanotwinned tungsten nanopillars: Effects of coherent twin boundary spacing, *Phys. Stat. Solidi RRL* 12 (2018) 1700399. URL: <https://onlinelibrary.wiley.com/doi/abs/10.1002/pssr.201700399>. doi:10.1002/pssr.201700399.
- [9] D. Hull, D. J. Bacon, *Introduction to Dislocations*, 5th ed., Butterworth-Heinemann, 2011.
- [10] R. Attree, J. Plaskett, XCI. The self-energy and interaction energy of stacking faults in metals, *Philos. Mag.* 1 (1956) 885–911.
- [11] A. Kumar, B. Kedjar, Y. Su, L. Thilly, I. J. Beyerlein, Atomic-level calculations and experimental study of dislocations in InSb, *J. Appl. Phys.* 127 (2020) 135104. URL: <https://aip.scitation.org/doi/10.1063/1.5139285>. doi:10.1063/1.5139285.
- [12] R. Peierls, The size of a dislocation, *Proc. Phys. Soc.* 52 (1940) 34–37. doi:10.1088/0959-5309/52/1/305.
- [13] B. Joós, M. Duesbery, The Peierls stress of dislocations: an analytic formula, *Phys. Rev. Lett.* 78 (1997) 266.
- [14] S. H. Haghigat, J. von Pezold, C. Race, F. Körmann, M. Friák, J. Neugebauer, D. Raabe, Influence of the dislocation core on the glide of the $1/2\langle 111 \rangle\{110\}$ edge

dislocation in bcc-iron: An embedded atom method study, *Comput. Mater. Sci* 87 (2014) 274–282.

[15] J. Christian, Some surprising features of the plastic deformation of body-centered cubic metals and alloys, *Metallurgical transactions A* 14 (1983) 1237–1256.

[16] S. Xu, Y. Su, L. T. W. Smith, I. J. Beyerlein, Frank-Read source operation in six body-centered cubic refractory metals, *J. Mech. Phys. Solids* 141 (2020) 104017. URL: <http://www.sciencedirect.com/science/article/pii/S0022509620302520>. doi:10.1016/j.jmps.2020.104017.

[17] S. L. Frederiksen, K. W. Jacobsen, Density functional theory studies of screw dislocation core structures in bcc metals, *Philos. Mag.* 83 (2003) 365–375. URL: <http://dx.doi.org/10.1080/014186102100034568>. doi:10.1080/014186102100034568.

[18] R. F. Zhang, J. Wang, I. J. Beyerlein, T. C. Germann, Twinning in bcc metals under shock loading: a challenge to empirical potentials, *Philos. Mag.* Lett. 91 (2011) 731–740. URL: <http://dx.doi.org/10.1080/09500839.2011.615348>. doi:10.1080/09500839.2011.615348.

[19] C. Yang, L. Qi, Modified embedded-atom method potential of niobium for studies on mechanical properties, *Comput. Mater. Sci.* 161 (2019) 351–363. URL: <http://www.sciencedirect.com/science/article/pii/S0927025619300473>. doi:10.1016/j.commatsci.2019.01.047.

[20] L. Yang, P. Söderlind, J. A. Moriarty, Accurate atomistic simulation of $(a/2)\langle 111 \rangle$ screw dislocations and other defects in bcc tantalum, *Philos. Mag. A* 81 (2001) 1355–1385.

- [21] X. Zhang, J. Tang, L. Deng, G. Zhong, X. Liu, Y. Li, H. Deng, W. Hu, The effects of interstitial impurities on the mechanical properties of vanadium alloys: A first-principles study, *J. Alloys Compd.* 701 (2017) 975–980. URL: <http://www.sciencedirect.com/science/article/pii/S0925838817301597>. doi:10.1016/j.jallcom.2017.01.135.
- [22] L. Romaner, C. Ambrosch-Draxl, R. Pippal, Effect of rhenium on the dislocation core structure in tungsten, *Phys. Rev. Lett.* 104 (2010) 195503. URL: <https://link.aps.org/doi/10.1103/PhysRevLett.104.195503>. doi:10.1103/PhysRevLett.104.195503.
- [23] M.-C. Marinica, L. Ventelon, M. R. Gilbert, L. Proville, S. L. Dudarev, J. Marian, G. Bencteux, F. Willaime, Interatomic potentials for modelling radiation defects and dislocations in tungsten, *J. Phys.: Condens. Matter* 25 (2013) 395502. URL: <http://stacks.iop.org/0953-8984/25/i=39/a=395502>. doi:10.1088/0953-8984/25/39/395502.
- [24] G. Bonny, D. Terentyev, A. Bakaev, P. Grigorev, D. V. Neck, Many-body central force potentials for tungsten, *Modelling Simul. Mater. Sci. Eng.* 22 (2014) 053001. URL: <http://stacks.iop.org/0965-0393/22/i=5/a=053001>. doi:10.1088/0965-0393/22/5/053001.
- [25] S. Xu, J. K. Startt, T. G. Payne, C. S. Deo, D. L. McDowell, Size-dependent plastic deformation of twinned nanopillars in body-centered cubic tungsten, *J. Appl. Phys.* 121 (2017) 175101. URL: <http://aip.scitation.org/doi/10.1063/1.4982754>. doi:10.1063/1.4982754.
- [26] J. Qian, C. Y. Wu, J. L. Fan, H. R. Gong, Effect of alloying elements on stacking fault energy and ductility of tungsten, *J. Alloys Compd.* 737

1
2
3
4
5
6 (2018) 372–376. URL: <http://www.sciencedirect.com/science/article/pii/S0925838817342172>. doi:10.1016/j.jallcom.2017.12.042.
7
8
9
10

11 [27] B. Bienvenu, C. C. Fu, E. Clouet, Impact of magnetism on screw dislocations in
12 body-centered cubic chromium, *Acta Mater.* 200 (2020) 570–580. URL: <http://www.sciencedirect.com/science/article/pii/S1359645420307357>.
13
14 doi:10.1016/j.actamat.2020.09.041.
15
16

17 [28] C. Woodward, S. Rao, *Ab-initio* simulation of isolated screw dislocations in bcc
18 Mo and Ta, *Philos. Mag. A* 81 (2001) 1305–1316.
19
20

21 [29] C. Woodward, S. Rao, Flexible *ab initio* boundary conditions: Simulating isolated
22 dislocations in bcc Mo and Ta, *Phys. Rev. Lett.* 88 (2002) 216402.
23
24

25 [30] F. Shimizu, S. Ogata, H. Kimizuka, T. Kano, J. Li, H. Kaburaki, First-principles
26 calculation on screw dislocation core properties in bcc molybdenum, *J. Earth Sim.*
27 7 (2007) 17–21.
28
29

30 [31] C. R. Weinberger, G. J. Tucker, S. M. Foiles, Peierls potential of screw dislocations
31 in bcc transition metals: Predictions from density functional theory, *Phys. Rev. B:*
32 *Condens. Matter* 87 (2013) 054114.
33
34

35 [32] L. Dezerald, D. Rodney, E. Clouet, L. Ventelon, F. Willaime, Plastic anisotropy and
36 dislocation trajectory in BCC metals, *Nat. Commun.* 7 (2016) 11695.
37
38

39 [33] L. Dezerald, L. Ventelon, E. Clouet, C. Denoual, D. Rodney, F. Willaime, *Ab*
40 *initio* modeling of the two-dimensional energy landscape of screw dislocations in
41 bcc transition metals, *Phys. Rev. B* 89 (2014) 024104. URL: <https://link.aps.org/doi/10.1103/PhysRevB.89.024104>.
42
43

- [34] D. Segall, A. Strachan, W. A. Goddard III, S. Ismail-Beigi, T. Arias, Ab initio and finite-temperature molecular dynamics studies of lattice resistance in tantalum, Phys. Rev. B: Condens. Matter 68 (2003) 014104.
- [35] S. Z. Chavoshi, S. Xu, Nanoindentation/scratching at finite temperatures: Insights from atomistic-based modeling, Prog. Mater. Sci. 100 (2019) 1–20. URL: <http://www.sciencedirect.com/science/article/pii/S0079642518300914>. doi:10.1016/j.pmatsci.2018.09.002.
- [36] S. Xu, Y. Su, D. Chen, L. Li, An atomistic study of the deformation behavior of tungsten nanowires, Appl. Phys. A 123 (2017) 788. URL: <https://link.springer.com/article/10.1007/s00339-017-1414-3>. doi:10.1007/s00339-017-1414-3.
- [37] S. Xu, Y. Su, S. Z. Chavoshi, Deformation of periodic nanovoid structures in Mg single crystals, Mater. Res. Express 5 (2018) 016523. URL: <http://stacks.iop.org/2053-1591/5/i=1/a=016523>. doi:10.1088/2053-1591/aaa678.
- [38] S. Xu, Y. Su, Dislocation nucleation from symmetric tilt grain boundaries in body-centered cubic vanadium, Phys. Lett. A 382 (2018) 1185–1189. URL: <http://www.sciencedirect.com/science/article/pii/S0375960118302287>. doi:10.1016/j.physleta.2018.03.002.
- [39] L. Proville, D. Rodney, M.-C. Marinica, Quantum effect on thermally activated glide of dislocations, Nature Mater. 11 (2012) 845–849. URL: <http://www.nature.com/nmat/journal/v11/n10/full/nmat3401.html>. doi:10.1038/nmat3401.
- [40] D. Dragoni, T. D. Daff, G. Csányi, N. Marzari, Achieving DFT accuracy with a

1
2
3
4
5
6 machine-learning interatomic potential: Thermomechanics and defects in bcc fer-
7
8 romagnetic iron, Phys. Rev. Mater. 2 (2018) 013808.
9

10 [41] P. Rowe, G. Csányi, D. Alfè, A. Michaelides, Development of a machine learning
11 potential for graphene, Phys. Rev. B: Condens. 97 (2018) 054303.
12

13 [42] V. Quaranta, J. Behler, M. Hellström, Structure and dynamics of the liquid–
14 water/zinc-oxide interface from machine learning potential simulations, J. Phys.
15 Chem. 123 (2018) 1293–1304.

16 [43] V. L. Deringer, G. Csányi, Machine learning based interatomic potential for amorphous
17 carbon, Phys. Rev. B: Condens. Matter 95 (2017) 094203.
18

19 [44] J. Byggmästar, K. Nordlund, F. Djurabekova, Gaussian approximation potentials for
20 body-centered-cubic transition metals, Phys. Rev. Mater. 4 (2020)
21 093802. URL: <https://link.aps.org/doi/10.1103/PhysRevMaterials.4.093802>.
22 doi:10.1103/PhysRevMaterials.4.093802.

23 [45] Y. Zuo, C. Chen, X. Li, Z. Deng, Y. Chen, J. Behler, G. Csányi, A. V. Shapeev,
24 A. P. Thompson, M. A. Wood, et al., Performance and cost assessment of machine
25 learning interatomic potentials, J. Phys. Chem. A 124 (2020) 731–745.
26

27 [46] C. Chen, Z. Deng, R. Tran, H. Tang, I.-H. Chu, S. P. Ong, Accurate force field for
28 molybdenum by machine learning large materials data, Phys. Rev. Mater. 1 (2017)
29 043603.
30

31 [47] A. P. Thompson, L. P. Swiler, C. R. Trott, S. M. Foiles, G. J. Tucker, Spectral neighbor
32 analysis method for automated generation of quantum-accurate interatomic po-
33 tentials, J. Comput. Phys. 285 (2015) 316–330.
34

- [48] Y. Su, M. Ardeljan, M. Knezevic, M. Jain, S. Pathak, I. J. Beyerlein, Elastic constants of pure body-centered cubic Mg in nanolaminates, *Comput. Mater. Sci.* 174 (2020) 109501. URL: <http://www.sciencedirect.com/science/article/pii/S0927025619308006>. doi:10.1016/j.commatsci.2019.109501.
- [49] S. Xu, E. Hwang, W.-R. Jian, Y. Su, I. J. Beyerlein, Atomistic calculations of the generalized stacking fault energies in two refractory multi-principal element alloys, *Intermetallics* 124 (2020) 106844.
- [50] S. Plimpton, Fast parallel algorithms for short-range molecular dynamics, *J. Comput. Phys.* 117 (1995) 1–19.
- [51] X. W. Zhou, R. A. Johnson, H. N. G. Wadley, Misfit-energy-increasing dislocations in vapor-deposited CoFe/NiFe multilayers, *Phys. Rev. B* 69 (2004) 144113. URL: <https://link.aps.org/doi/10.1103/PhysRevB.69.144113>. doi:10.1103/PhysRevB.69.144113.
- [52] D.-Y. Lin, S. S. Wang, D. L. Peng, M. Li, X. D. Hui, An n -body potential for a Zr-Nb system based on the embedded-atom method, *J. Phys.: Condens. Matter* 25 (2013) 105404. URL: [https://doi.org/10.1088/0953-8984/25/10/105404](https://doi.org/10.1088%2F0953-8984%2F25%2F10%2F105404). doi:10.1088/0953-8984/25/10/105404.
- [53] S. Xu, Y. Su, W.-R. Jian, I. J. Beyerlein, Local slip resistances in equal-molar MoNbTi multi-principal element alloy, *Acta Mater.* 202 (2021) 68–79. URL: <http://www.sciencedirect.com/science/article/pii/S1359645420308405>. doi:10.1016/j.actamat.2020.10.042.
- [54] Y. N. Osetsky, D. J. Bacon, An atomic-level model for studying the dynamics of edge dislocations in metals, *Modelling Simul. Mater. Sci. Eng.* 11 (2003) 427.

- 1
2
3
4
5
6 [55] S. Xu, J. R. Mianroodi, A. Hunter, I. J. Beyerlein, B. Svendsen, Phase-field-based
7 calculations of the disregistry fields of static extended dislocations in FCC metals,
8 Phil. Mag. 99 (2019) 1400–1428.
9
10
11
12 [56] S. Xu, L. Smith, J. R. Mianroodi, A. Hunter, B. Svendsen, I. J. Beyerlein, A com-
13 parison of different continuum approaches in modeling mixed-type dislocations in
14 Al, Modelling Simul. Mater. Sci. Eng. 27 (2019) 074004.
15
16
17 [57] S. Xu, Y. Su, I. J. Beyerlein, Modeling dislocations with arbitrary character angle
18 in face-centered cubic transition metals using the phase-field dislocation dynamics
19 method with full anisotropic elasticity, Mech. Mater. 139 (2019) 103200.
20
21
22 [58] W.-R. Jian, M. Zhang, S. Xu, I. J. Beyerlein, Atomistic simulations of dynamics of
23 an edge dislocation and its interaction with a void in copper: a comparative study,
24 Modelling Simul. Mater. Sci. Eng. 28 (2020) 045004. URL: <https://doi.org/10.1088/1361-651X/ab8358>. doi:10.1088/1361-651X/ab8358.
25
26
27 [59] A. Stukowski, Visualization and analysis of atomistic simulation data with OVITO—
28 the Open Visualization Tool, Modell. Simul. Mater. Sci. Eng. 18 (2009) 015012.
29
30
31 [60] A. Stukowski, Structure identification methods for atomistic simula-
32 tions of crystalline materials, Modelling Simul. Mater. Sci. Eng. 20
33 (2012) 045021. URL: <https://doi.org/10.1088/0965-0393/20/4/045021>. doi:10.1088/0965-0393/20/4/045021.
34
35
36 [61] E. Bitzek, P. Koskinen, F. Gähler, M. Moseler, P. Gumbsch, Structural relaxation
37 made simple, Phys. Rev. Lett. 97 (2006) 170201.
38
39
40 [62] M. Duesbery, V. Vitek, Plastic anisotropy in b.c.c. transition metals, Acta Mater. 46
41 (1998) 1481–1492.
42
43
44
45
46
47
48
49
50
51
52
53
54
55
56
57
58
59
60
61
62
63
64
65

- 1
2
3
4
5
6 [63] G. Ackland, R. Thetford, An improved n-body semi-empirical model for body-
7 centred cubic transition metals, *Philos. Mag. A* 56 (1987) 15–30.
8
9
10 [64] W.-R. Jian, S. Xu, I. J. Beyerlein, On the significance of model design
11 in atomistic calculations of the Peierls stress in Nb, *Comput. Mater. Sci.*
12 (2021) 110150. URL: <http://www.sciencedirect.com/science/article/pii/S0927025620306418>. doi:10.1016/j.commatsci.2020.110150.
13
14
15 [65] K.-I. Masuda, A. Sato, Electronic theory for screw dislocation in BCC transition
16 metals: Calculation of the peierls stress and the core energy, *Philos. Mag. B* 37
17 (1978) 531–536.
18
19 [66] X.-G. Li, C. Chen, H. Zheng, Y. Zuo, S. P. Ong, Complex strengthening mecha-
20 nisms in the NbMoTaW multi-principal element alloy, *npj Comput. Mater.* 6 (2020)
21 70.
22
23 [67] H. Park, M. R. Fellinger, T. J. Lenosky, W. W. Tipton, D. R. Trinkle, S. P. Rudin,
24 C. Woodward, J. W. Wilkins, R. G. Hennig, *Ab initio* based empirical potential used
25 to study the mechanical properties of molybdenum, *Phys. Rev. B: Condens. Matter*
26 85 (2012) 214121.
27
28 [68] K. Kang, V. V. Bulatov, W. Cai, Singular orientations and faceted motion of dislo-
29 cations in body-centered cubic crystals, *Proc. Natl. Acad. Sci. U.S.A.* 109 (2012)
30 15174–15178.
31
32 [69] J. Li, C.-Z. Wang, J.-P. Chang, W. Cai, V. V. Bulatov, K.-M. Ho, S. Yip, Core energy
33 and Peierls stress of a screw dislocation in bcc molybdenum: A periodic-cell tight-
34 binding study, *Phys. Rev. B: Condens. Matter* 70 (2004) 104113.
35
36
37
38
39
40
41
42
43
44
45
46
47
48
49
50
51
52
53
54
55
56
57
58
59
60
61
62
63
64
65

- 1
2
3
4
5
6 [70] M. Mrovec, D. Nguyen-Manh, D. G. Pettifor, V. Vitek, Bond-order potential for
7 molybdenum: Application to dislocation behavior, *Phys. Rev. B: Condens. Matter*
8 69 (2004) 094115.
- 9
10
11
12
13 [71] J. A. Moriarty, V. Vitek, V. V. Bulatov, S. Yip, Atomistic simulations of dislocations
14 and defects, *J. Comput.-Aided Mater. Des.* 9 (2002) 99–132. URL: <https://doi.org/10.1023/A:1026022602578>. doi:10.1023/A:1026022602578.
- 15
16
17
18 [72] S. Rao, C. Woodward, Atomistic simulations of $(a/2) \langle 111 \rangle$ screw dislocations in
19 bcc Mo using a modified generalized pseudopotential theory potential, *Philos. Mag. A* 81 (2001) 1317–1327.
- 20
21
22
23
24
25
26 [73] J. A. Moriarty, Analytic representation of multi-ion interatomic potentials in transi-
27 tion metals, *Phys. Rev. B* 42 (1990) 1609–1628. URL: <https://link.aps.org/doi/10.1103/PhysRevB.42.1609>. doi:10.1103/PhysRevB.42.1609.
- 28
29
30
31
32 [74] W. Xu, J. A. Moriarty, Accurate atomistic simulations of the Peierls barrier and
33 kink-pair formation energy for $\langle 111 \rangle$ screw dislocations in bcc Mo, *Comput. Mater.
34 Sci.* 9 (1998) 348–356.
- 35
36
37
38
39 [75] J. A. Moriarty, W. Xu, P. Söderlind, J. Belak, L. H. Yang, J. Zhu, Atom-
40 istic simulations for multiscale modeling in bcc metals, *J. Eng. Mater. Tech.* 121 (1999)
41 120–125. URL: <https://asmedigitalcollection.asme.org/materialstechnology/article/121/2/120/403376/Atomistic-Simulations-for-Multiscale-Modeling-in>. doi:10.1115/1.2812355.
- 42
43
44
45
46
47
48
49
50
51
52 [76] K. Ito, V. Vitek, Atomistic study of non-Schmid effects in the plastic yielding of
53 bcc metals, *Philos. Mag. A* 81 (2001) 1387–1407.
- 54
55
56
57
58
59
60
61
62
63
64
65

- [77] H. Haas, C. Z. Wang, M. Fähnle, C. Elsässer, K. M. Ho, Environment-dependent tight-binding model for molybdenum, *Phys. Rev. B* 57 (1998) 1461–1470. URL: <https://link.aps.org/doi/10.1103/PhysRevB.57.1461>. doi:10.1103/PhysRevB.57.1461.
- [78] D. Vanderbilt, Soft self-consistent pseudopotentials in a generalized eigenvalue formalism, *Phys. Rev. B* 41 (1990) 7892–7895. URL: <https://link.aps.org/doi/10.1103/PhysRevB.41.7892>. doi:10.1103/PhysRevB.41.7892.
- [79] G. Kresse, D. Joubert, From ultrasoft pseudopotentials to the projector augmented-wave method, *Phys. Rev. B: Condens. Matter* 59 (1999) 1758.
- [80] L. Hollang, D. Brunner, A. Seeger, Work hardening and flow stress of ultrapure molybdenum single crystals, *Mater. Sci. Eng., A* 319 (2001) 233–236.
- [81] Y. Aono, E. Kuramoto, K. Kitajima, Fundamental plastic behaviors in high-purity bcc metals (Nb, Mo and Fe), in: Strength of Metals and Alloys (ICSMA 6), Elsevier, 1982, pp. 9–14.
- [82] L. M. Hale, J. A. Zimmerman, C. R. Weinberger, Simulations of bcc tantalum screw dislocations: Why classical inter-atomic potentials predict {112} slip, *Comput. Mater. Sci.* 90 (2014) 106–115.
- [83] M. R. Fellinger, H. Park, J. W. Wilkins, Force-matched embedded-atom method potential for niobium, *Phys. Rev. B* 81 (2010) 144119.
- [84] S. Takeuchi, T. Hashimoto, K. Maeda, Plastic deformation of bcc metal single crystals at very low temperatures, *Trans. Jpn. Inst. Met.* 23 (1982) 60–69.
- [85] D. Segall, T. Arias, A. Strachan, W. Goddard, Accurate calculations of the Peierls stress in small periodic cells, *J. Comput.-Aided Mater. Des.* 8 (2001) 161–172.

- 1
2
3
4
5
6 [86] A. Strachan, T. Çağın, O. Gülseren, S. Mukherjee, R. E. Cohen, W. A. Goddard III,
7 First principles force field for metallic tantalum, *Modelling Simul. Mater. Sci. Eng.*
8 12 (2004) S445–S459. URL: <https://doi.org/10.1088/0965-0393/12/4/S10>.
9
10
11
12
13
14 [87] A. Guellil, J. Adams, The application of the analytic embedded atom method to bcc
15 metals and alloys, *J. Mater. Res.* 7 (1992) 639–652.
16
17
18 [88] Y. Li, D. J. Siegel, J. B. Adams, X.-Y. Liu, Embedded-atom-method tantalum potential developed by the force-matching method, *Phys. Rev. B* 67 (2003)
19 125101. URL: <https://link.aps.org/doi/10.1103/PhysRevB.67.125101>.
20 doi:10.1103/PhysRevB.67.125101.
21
22
23
24 [89] X. Zhou, H. Wadley, R. A. Johnson, D. Larson, N. Tabat, A. Cerezo, A. Petford-
25 Long, G. Smith, P. Clifton, R. Martens, et al., Atomic scale structure of sputtered
26 metal multilayers, *Acta Mater.* 49 (2001) 4005–4015.
27
28
29 [90] Y. Mishin, A. Lozovoi, Angular-dependent interatomic potential for tantalum, *Acta*
30 *Mater.* 54 (2006) 5013–5026.
31
32
33
34 [91] G. Wang, A. Strachan, T. Cagin, W. A. Goddard III, Molecular dynamics simulations of $1/2a\langle 111 \rangle$ screw dislocation in Ta, *Mater. Sci. Eng., A* 309 (2001)
35 133–137.
36
37
38
39 [92] G. Wang, A. Strachan, T. Çağın, W. A. Goddard III, Calculating the Peierls energy and Peierls stress from atomistic simulations of screw dislocation dynamics:
40 application to bcc tantalum, *Modell. Simul. Mater. Sci. Eng.* 12 (2004) S371.
41
42
43
44
45
46 [93] C. Woodward, S. Kajihara, L. H. Yang, Site preferences and formation energies of
47 substitutational Si, Nb, Mo, Ta, and W solid solutions in $L1_0$ Ti-Al, *Phys. Rev. B* 57
48
49
50
51
52
53
54
55
56
57
58
59
60
61
62
63
64
65

1
2
3
4
5
6 (1998) 13459–13470. URL: <https://link.aps.org/doi/10.1103/PhysRevB.57.13459>.
7
8
9

10 [94] S. Takeuchi, K. Maeda, Slip in high purity tantalum between 0.7 and 40 K, *Acta*
11 *Metall.* 25 (1977) 1485–1490.
12
13

14 [95] D. Brunner, J. Diehl, V. Glebovsky, The plastic behavior of high-purity tungsten,
15 in: *Proceedings of the 5th International Conference on Ultra High-Purity Materials*,
16 1998, pp. 83–92.
17
18

19 [96] R. Gröger, V. Vitek, Explanation of the discrepancy between the measured and
20 atomistically calculated yield stresses in body-centred cubic metals, *Philos. Mag.*
21 Lett. 87 (2007) 113–120.
22
23

24 [97] T. Suzuki, H. Koizumi, Inertial motion and multi-kink pair formation of dislocations
25 on the Peierls potential, *Philos. Mag. A* 67 (1993) 1153–1160.
26
27

28 [98] D. Caillard, Kinetics of dislocations in pure Fe. Part I. In situ straining experiments
29 at room temperature, *Acta Mater.* 58 (2010) 3493–3503.
30
31

32 [99] D. Caillard, Kinetics of dislocations in pure Fe. Part II. In situ straining exper-
33 iments at low temperature, *Acta Mater.* 58 (2010) 3504 – 3515. URL: <http://www.sciencedirect.com/science/article/pii/S1359645410001102>.
34 doi:<https://doi.org/10.1016/j.actamat.2010.02.024>.
35
36

37 [100] S. Z. Xu, Z. M. Hao, Y. Q. Su, Y. Yu, Q. Wan, W. J. Hu, An analysis on nanovoid
38 growth in body-centered cubic single crystalline vanadium, *Comput. Mater.*
39 *Sci.* 50 (2011) 2411–2421. URL: <http://www.sciencedirect.com/science/article/pii/S0927025611001625>. doi:[10.1016/j.commatsci.2011.03.019](https://doi.org/10.1016/j.commatsci.2011.03.019).
40
41
42
43
44
45
46
47
48
49
50
51
52
53
54
55
56
57
58
59
60
61
62
63
64
65

- 1
2
3
4
5
6 [101] S. Xu, Y. Su, Nanovoid growth in BCC α -Fe: influences of initial void geometry,
7 Modelling Simul. Mater. Sci. Eng. 24 (2016) 085015. URL: <http://stacks.iop.org/0965-0393/24/i=8/a=085015>. doi:10.1088/0965-0393/24/8/085015.
8
9
10
11
12
13
14
15
16
17
18
19
20
21
22
23
24
25
26
27
28
29
30
31
32
33
34
35
36
37
38
39
40
41
42
43
44
45
46
47
48
49
50
51
52
53
54
55
56
57
58
59
60
61
62
63
64
65

Declaration of interests

The authors declare that they have no known competing financial interests or personal relationships that could have appeared to influence the work reported in this paper.

The authors declare the following financial interests/personal relationships which may be considered as potential competing interests: